On the influence of varying the crystallographic texture of alumina CVD coatings on cutting performance in steel turning

International Journal of Machine Tools & Manufacture 176 (2022) 103885

Contents lists available at ScienceDirect

International Journal of Machine Tools and Manufacture

journal homepage: www.elsevier.com/locate/ijmactool

On the influence of varying the crystallographic texture of alumina CVD coatings on cutting performance in steel turning

S. Shoja [a,b,*], S. Norgren [b,c], H.-O. Andrén [a], O. Bäcke [a], M. Halvarsson [a]

[a] Department of Physics, Chalmers University of Technology, Gothenburg, Sweden
[b] Sandvik Coromant R&D, Stockholm, Sweden
[c] Department of Mechanical Engineering Sciences, Lund University, Lund, Sweden

ARTICLE INFO

Keywords:
α-Al_2O_3
Hard coatings
CVD
Crater wear
Machining
Texture

ABSTRACT

Understanding the mechanisms at the tool/chip interface during metal cutting is crucial in the production of almost every metallic component used in engineering applications. It is critical to have rapid, durable, and reliable machining processes. This work contributes to the understanding of mechanisms occurring on the tool in the secondary shear zone, and it is focusing on the tool side of the contact. Crystallographic textured Chemical Vapor Deposited (CVD) α-Al_2O_3 coated cutting tools are dominating the steel turning area, as they show an increased performance compared to coatings with randomly oriented grains. In this study, we investigate the effect of three different CVD α-Al_2O_3 textures on the initial rake crater behavior. This was done using a turning test designed to generate crater wear only in the alumina layer, which was deposited onto an inner Ti(C,N) layer, which in turn was deposited on a cemented carbide insert. With this approach, the influence of the underlying coating layer and substrate was reduced. Pre- and post-machining characterization of the different contact areas on the surfaces of the three textured CVD α-Al_2O_3 coatings, (0001)(0001), $(01\bar{1}2)$ and $(11\bar{2}0)$, was performed using scanning electron microscopy (SEM), electron backscattered diffraction (EBSD) and energy dispersive X-ray spectroscopy (XEDS). Plastic deformation, micro-rupture, abrasion and chemical reactions with the work-piece material are all identified as mechanisms involved in crater formation during turning. For the (0001)-textured coating, the observed low wear-rate is attributed to homogeneous basal-slip dominating plastic deformation, while for the $(01\bar{1}2)$ and $(11\bar{2}0)$ textures the main deformation mechanisms are attributed to heterogeneous plastic deformation, causing micro-rupture and abrasion, leading to higher wear-rates. The effect of a larger coating grain size is mainly seen as the formation of wider ridges and valleys, while the effect on wear rate was limited.

1. Introduction

Understanding the mechanisms at the tool/chip interface during metal cutting is crucial in the production of almost every metallic component used in engineering applications [1]. It is critical to have rapid, durable, and reliable machining processes in order to achieve a high level of productivity in a production line. One source of process disturbance is the wear of the cutting tools in steel turning machining, and severe material deformation takes place in both the workpiece and chip as well as on the tool surface. Usually, three distinct regions are defined, where high temperature and strain locally develop at extreme rates [2]. These are: (a) primary shear zone constituted by fast shearing metal volumes from the workpiece during chip formation; (b) secondary shear zone, progressing by friction at the tool-chip contact; (c) tertiary shear zone, where plastic deformation in the new machined workpiece occurs due to the contact with the tool flank. In this work we have focused on contributing to the understanding of the mechanisms occurring on the tool in the secondary shear zone, and the focus was also on the tool side of the contact.

Multi-layered coatings greatly enhance cutting tool performance and tool life [3–6]. Here, in particular, CVD (Chemical Vapor Deposition) α-alumina coatings are outstanding in steel turning applications, partly due to their stability and chemical inertness [7]. During the latest 15 years, research has been focused on crystallographically textured α-Al_2O_3 coatings [8], as they exhibit an increased performance compared to coatings with randomly oriented grains. Note that the term

* Corresponding author. Department of Physics, Chalmers University of Technology, Gothenburg, Sweden.
E-mail address: siamak.shoja@sandvik.com (S. Shoja).

https://doi.org/10.1016/j.ijmachtools.2022.103885
Received 22 December 2021; Received in revised form 31 March 2022; Accepted 2 April 2022
Available online 10 April 2022

"textured insert" is also used for micro-texturing of the insert surface that may serve as "micro-pools for lubricants" enhancing the tribological behavior [9,10]. However, the texture in our study refers to the crystallographic texture of the coatings. Ruppi [11] and M'Saoubi and Ruppi [12] investigated different textures, $(01\bar{1}2)$, $(10\bar{1}4)$, (0001), and Ruppi also $(10\bar{1}0)$ [11], and found that the (0001)-textured coatings outperformed the others in steel turning with respect to tool life. It was assumed that the best wear resistance was achieved when many (0001) crystallographic planes of the α-Al_2O_3 layer were oriented parallel to the coating surface [11,12]. Therefore, the focus has since then been on how to control and increase the (0001) texture in these types of coatings.

It is desired to keep enhancing the performance of the coating materials. In order to do this, a thorough understanding of the basic wear mechanisms is essential. The wear during turning takes place on both the clearance and the rake side of the cutting tool insert. While flank wear develops on the clearance side, crater wear develops on the rake side, where the chip is in contact with the insert. Crater wear is suggested to be a result of a combination of plastic deformation, abrasive and chemical wear [11–21]. It is well known that different parameters, e.g. cutting speed, feed, depth of cut, and type of workpiece material as well as amount and type of inclusions in the workpiece material affect the degree and type of wear on the cutting tool [18,20,22,23]. However, the impact of the Al_2O_3-coating texture has not been given enough consideration. In this work, we concentrate on the crater formation in the alumina part of multilayer (TiCN + α-Al_2O_3) textured coatings, which is therefore the aim of this paper.

Dearnley reported a wear pattern for untextured alumina coatings that at higher magnifications appeared as ridges and valleys on the rake face [13]. The rate of ridge formation was found to increase with increasing cutting speed and was most noticeable at some distance from the cutting edge, where the generated temperatures are the highest [24,25], This was later also observed by M'Saoubi et al. [19] for textured α-Al_2O_3 coatings. It was proposed that ridge formation is a temperature-dependent process and that elongated ridges are formed in the chip flow direction by plastic deformation of the alumina surface region [13]. Goh et al. [22] proposed plastic deformation-induced necking of asperities as the cause for the long and parallel ridges observed on the rake face (crater wear) in their work of untextured alumina inserts.

Many authors suggest abrasion as the main cause for the formation of valleys and ridges, possibly by particles and inclusions in the workpiece material abrading the coating material, producing deformation and material removal [18,26–29]. However, the ridges were mainly formed on the flank side and the coatings usually wore down to the layers underneath which might also contribute to the abrasive wear. In the study by M'Saoubi and co-workers [19] on (0001), $(01\bar{1}2)$, and $(10\bar{1}0)$ textures, ridges and valleys were observed in the transition and sliding zones for all textures, which were interpreted as a sign of plastic deformation. In addition, they observed a high dislocation density close to the worn surface that supported this claim. By using data for the temperature dependence for slip system activation [30–32] they showed that basal slip is the most probable slip system to be active in their experiments at a high cutting speed of 300 m/min, thus generating plastic flow. The Schmid factor and thus the resolved shear stress for basal slip is higher for (0001) than for $(01\bar{1}2)$ and $(10\bar{1}0)$ textures, which should give a more uniform plastic flow in (0001)-textured coatings. The grains in $(01\bar{1}2)$ and $(10\bar{1}0)$ textured coatings are less favorably oriented for basal slip, resulting in lower Schmid factor values, leading to lower resolved shear stress and limited plastic flow prior to possible coating fracture. This would result in poorer performance [11,12,19]. However, in their extensive work [19] a single Schmid factor value was considered for the whole chip/tool contact as a first approximation. This results in an overestimation of the resolved shear stress (in zone I) and a general disregard for lateral rotation of fiber-textured grains, which gives large variations of Schmid factor values for the individual grains, especially in the $(01\bar{1}2)$ and $(10\bar{1}0)$–textured coatings, as shown in our previous study [33]. Plausibly this overestimation of resolved shear stress also has the potential to alter the proposed wear mechanisms, especially in zone I.

The aim of this paper is to increase the understanding of the influence of CVD α-Al_2O_3 coating texture on initial crater formation on the cutting tool inserts during steel turning. This is done by detailed observations and analyses of different wear zones on the surfaces of three different coating textures, (0001), $(01\bar{1}2)$ and $(11\bar{2}0)$ using scanning electron microscope (SEM) investigations, including electron backscattered diffraction (EBSD), energy dispersive X-ray spectroscopy (XEDS) and focused ion beam (FIB) cross-sectioning. By comparing surface morphologies of different coating textures and linking them to the observed deformation, an increased understanding of the wear mechanisms will be presented.

2. Materials and methods

2.1. Materials and electron microscopy characterizations

All coatings were deposited on inserts of ISO CNMG120408-PM geometry of the same grade of cemented carbide, consisting of 76.3 vol% WC, 12.4 vol% Co-rich binder phase, and 11.3 vol% cubic carbide (Ti, Ta, Nb, W)(C, N). It had been gradient sintered to give a 25 μm thick surface layer devoid of hard cubic carbide and enriched in tough binder phase, to prevent any cracks in the coating to propagate into the bulk of the substrate. The coatings were made using an industrial scale hot-wall CVD of type Bernex 530 L, with overall dimensions of 1600 mm height and 530 mm diameter and a batch capacity of 10,000 inserts. The coatings were composed of several sublayers obtained from distinct manufacturing steps. They consisted of an inner TiN layer, ~0.3 μm thick, deposited at 930 °C, followed by a medium temperature CVD Ti(C, N) layer with a thickness of ~6 μm, deposited at 885 °C from $TiCl_4$ and CH_3CN. Then a bonding layer (Ti(C,N,O)) with a thickness of ~0.5 μm was deposited at 1000 °C using $TiCl_4$, N_2, CH_3CN and CO, followed by a ~5 μm thick α-Al_2O_3 layer deposited at 1000 °C with a specific texture, either (0001), $(01\bar{1}2)$ or $(11\bar{2}0)$ using $AlCl_3$, CO_2 and H_2 as precursors together with additions of different amounts of H_2S and CO during the nucleation and growth steps [8,11,34,35]. These three coatings are referred to as Sample (001), Sample (012) and Sample (110), respectively.

Scanning Electron Microscopy (SEM) was used to examine the microstructure of the samples. At the three different wear zones (sticking, transition and sliding zone) on the rake face, special consideration was devoted to the surface topography of the machined alumina layers. The chemical composition was determined by Energy Dispersive X-ray Spectroscopy (EDS) using an Oxford Aztec system. Both as-deposited and machined inserts were examined using a Zeiss Ultra Field Emission Gun (FEG) SEM, operated at 10 kV. Based on Electron Backscattered Diffraction (EBSD) data, the texture of the as-deposited α-Al_2O_3 coatings near the cutting corner on the rake face was investigated using pole figure analysis. The surface roughness of the coatings in the sliding zone and their corresponding chips were analyzed using SEM stereoscopic images along with the Alicona MeX software package, which uses stereoscopic images to retrieve 3D information and generate a 3D dataset. This was then used to perform profile and roughness measurements. The machining tests, specimen preparation, imaging and analytical methods are described in detail below.

2.2. Metal cutting experiments

Three differently textured coatings were evaluated utilizing a modern Computerized Numerical Control (CNC) lathe by machining a steel workpiece material in single point dry turning. The inserts were used in longitudinal dry turning for 2 min in cut. This turning test was designed

to only occur in the alumina part of the multi-layered coatings in order to investigate the influence of alumina coating textures. The same cutting parameters and workpiece material were used for all cases; a cutting speed (v_c) of 220 m/min, a feed rate (f) of 0.2 mm/rev and a depth of cut (a_p) of 2 mm were employed and the chips were collected for analysis. The workpiece material used was Ovako 825 B, a non-Ca-treated 100CrMo7-3 bearing steel in the soft annealed condition. The chemical composition according to the certificate was C: 0.96, Si: 0.26, Mn: 0.67, Cr: 1.67, Ni: 0.15, Mo: 0.23, Al: 0.034, O: 4.5 ppm Ti: 12 ppm, S: 0.007, P:0.012 (wt.% if not given in ppm) and the hardness was 205 HB. Additionally, the cutting forces were measured using a Kistler device when turning using twin inserts with identical geometry and coating, and using the same workpiece material and cutting conditions.

2.3. Focused Ion Beam/Scanning Electron Microscopy and Transmission Kikuchi Diffraction

An FEI Versa 3D combined Focused Ion Beam/Scanning Electron Microscope (FIB/SEM) workstation was used to produce cross-sections and thin-foils from the coatings and subjacent substrates. The thin-foils were later used for overview microstructure analysis using Scanning Transmission Electron Microscope (STEM) and Transmission Kikuchi Diffraction (TKD) in the SEM, see below, while the cross-sections were used for local coating thickness determination. In order to protect the surface from ion beam damage, a thin Pt-layer with a thickness of around 100 nm was first deposited onto the surface (25 μm long and 5 μm wide) using the electron beam and then a thicker Pt layer (~2 μm) was deposited on top with the assistance of Ga-ions. Low accelerating voltages, i.e. 5 kV and 2 kV, with ion currents of 50 pA and 30 pA, were used in the final thinning process, in order to minimize the ion beam-induced damage.

Grain orientation mapping of the alumina layers was performed by means of TKD using an HKL Channel 5 EBSD system with a Nordlys II detector, mounted on a Tescan GAIA3 FIB/SEM instrument. The TKD data were collected from the FIB/SEM-prepared thin-foils. An accelerating voltage of 30 kV in the high current mode, an aperture size of 120 μm and a step size of 15–25 nm were used.

2.4. Electron backscatter diffraction

EBSD was used to analyze the grain orientations at the surface of the as-deposited alumina layers. This allowed the determination of the grain size and shape, as well as the local texture of the three samples. The investigations were carried out using an Oxford Aztec EBSD system with a NordlysNano detector, mounted on the Tescan GAIA3 FIB/SEM instrument. Areas of 50 μm × 50 μm with a 200 nm step size were investigated using 20 kV operating voltage, which was adequate to obtain good statistics. The HKL Channel 5 (Oxford Instruments) software was used for data analysis.

3. Results

3.1. As-deposited coatings

The surface morphologies of the as-deposited CVD α-alumina coatings with the three different textures, (0001), $(01\bar{1}2)$ and $(11\bar{2}0)$, i.e. Sample (001), Sample (012) and Sample (110), are shown in Fig. 1a–c, respectively. The coatings have relatively similar morphologies, with grains exhibiting several relatively flat facets. However, the coatings do not have the same grain size. To measure the size distribution and also map the orientations of the grains, EBSD analysis was performed on the rake face of the coated inserts. The equivalent circle diameter method was used to measure the grain size distributions of the three coatings, and the results are shown in Fig. 1df. It can be observed that Sample (001) and (012) have smaller grains of 1.4 ± 0.5 μm and 1.4 ± 0.4 μm respectively (Figs. 1d and e), compared to 2 ± 0.8 μm for Sample (110), see Fig. 1f. Much larger grains, measuring 5–6 μm in diameter, could also be found locally in Sample (110).

Fig. 2a shows {0001}, $\{01\bar{1}2\}$ and $\{11\bar{2}0\}$ pole figures for the three textured coatings, i.e. Sample (001), Sample (012) and Sample (110),

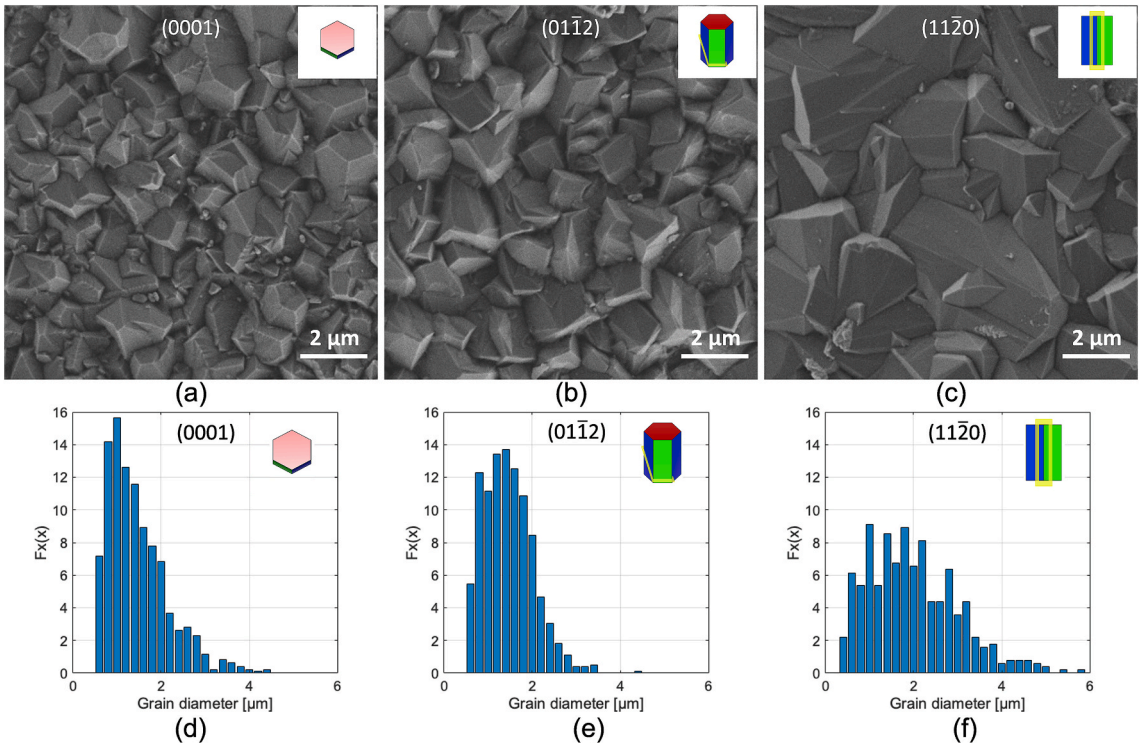

Fig. 1. SEM secondary electron micrographs showing the surface morphologies of the three CVD α-alumina coatings; (a) Sample (001), (b) Sample (012) and (c) Sample (110). (d–f) The grain size distribution for Sample (001), Sample (012) and Sample (110), respectively.

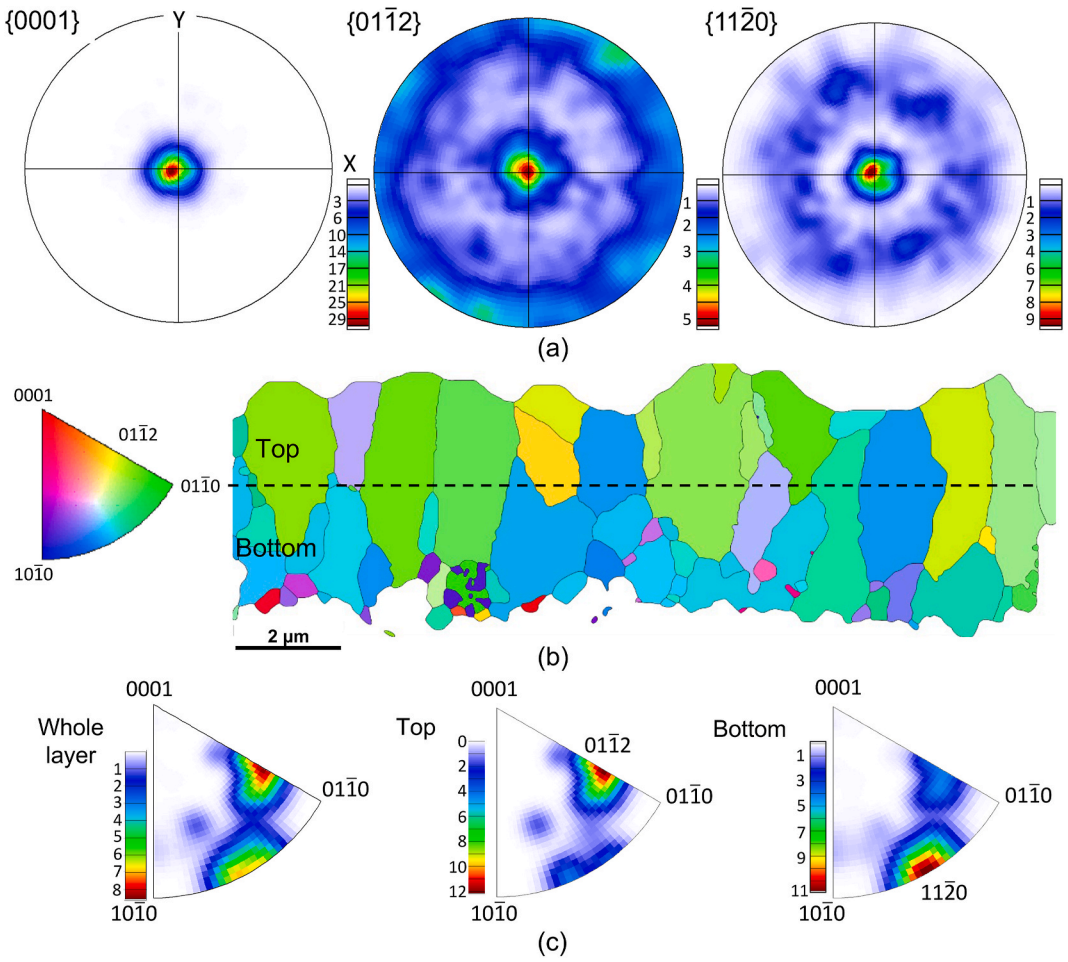

Fig. 2. (a) Pole figure plots obtained from EBSD data from the surfaces of Samples (001), (012) and (110). Pole figure plots {0001}, {01$\bar{1}$2} and {11$\bar{2}$0} show the orientation distributions for the grains in Samples (001), (012) and (110), respectively. (b) TKD cross-section inverse pole figure map for Sample (012) showing the mean orientation of each grain. (c) Inverse pole figures extracted from the IPF map for the whole, top and bottom parts of the coating, showing a dual texture. The grains are aligned (parallel to the surface) towards (01$\bar{1}$2) in the top half and more aligned towards (11$\bar{2}$0) in the bottom half of the coating.

retrieved from EBSD data. The center of the {0001} pole figure for Sample (001) shows a high intensity, indicating that the majority of the grains in this sample have an (0001) orientation (parallel to the surface). The {11$\bar{2}$0} pole figure for Sample (110) shows a high intensity in the center and a ring at 60°, indicating that most of the grains have a (11$\bar{2}$0) orientation. The {01$\bar{1}$2} pole figure for Sample (012) shows some intensities at the center (not as high as for the other two samples) and a hint of an intensity ring at 90°, as well as some scattered intensities in the area between the center and periphery. This implies that the coating texture of Sample (012) is slightly weaker than that of the other two coatings.

In order to further investigate the weaker texture in Sample (012), TKD was performed on a cross-section lift-out lamella, in order to study the texture as a function of coating height. Inverse pole figures (IPFs) and an IPF map obtained from the alumina layer are shown in Fig. 2b and c. The IPFs were taken both from the whole layer, as well as from the upper and lower halves. It is clear from the IPF extracted from the whole layer that the (01$\bar{1}$2) alumina layer contains a dual texture. It can be observed from the IPFs obtained from the upper and lower halves that (01$\bar{1}$2) texture is more dominant in the top part, while the lower part exhibits more (11$\bar{2}$0) texture. The results from the top part agree with the pole figure (Fig. 2a) obtained using EBSD on the surface of Sample (012), since that data is originating from the outermost 50 nm of the alumina layer. As the outer part of the coating is most significant when it comes to the wear in our relatively short machining tests, Sample (012) can be considered as primarily degraded in the (01$\bar{1}$2) textured part of this coating.

3.2. Crater wear and adhered workpiece material

As mentioned in section 2.2, ISO CNMG120408-PM inserts with three different CVD alumina coating textures were used to turn a bearing steel for 2 min. Cutting forces were determined during longitudinal turning of the same workpiece material and with the same cutting parameters. Tangential and feed forces are reported in Table 1, which

Table 1
Measured cutting forces including tangential force F_t and feed force F_f and calculated normal (compressive) stresses considering both the total contact area and the area of edge and sticking zone on the rake face for Samples (001), (012) and (110).

	Measured forces		Averagenormal stress	Sticking zonenormal stress
	F_t [N]	F_f [N]	σ [MPa]	σ [MPa]
Sample (001)	980 ± 30	460 ± 20	1110 ± 70	2660 ± 160
Sample (012)	1000 ± 30	490 ± 20	1120 ± 70	2690 ± 160
Sample (110)	1000 ± 30	500 ± 15	1140 ± 70	2720 ± 160

generally show that the tangential force is about twice as large as the feed force for all three samples and the differences between measured forces for different samples are marginal. In order to interpret the variation in the tribological behavior of the α-alumina layers, it is worth estimating the contributions of normal stresses on the tool rake face. It should be mentioned that due to the chip-breaker and the tool/chip contact geometry, the forces are not evenly distributed over the whole contact surface and that the forces are lower than the case without chip-breaker [36]. Thus, the insert edge and zone I take more compressive forces than zone III [2,37]. Assuming that the tangential forces are applied on the total contact area [measured to 0.885 $mm^2 \pm 5\%$], given in Fig. 3a, the compressive stresses can be calculated. However, since most of the tangential forces are applied on the edge and sticking zone the calculated stresses are underestimated. A better estimation thus would be to calculate the compressive stresses for the edge and sticking zone area [0.37 $mm^2 \pm 5\%$], given in Fig. 3b. The calculated stresses considering the total contact area and only the edge and sticking zone area (brighter area showing the adhered workpiece material) are reported in Table 1.

It was not possible to determine the temperatures in our experiment since longitudinal turning was used in this work. This makes it impossible for the thermal camera to face the cutting zone and the rake face of the insert. However, it would be valuable to estimate the temperatures on the rake face of the insert during cutting. It is known that the temperature on the rake face is highest at a distance from the edge [38]. FEM (Finite Element Method) modeling performed for the rake face of the ISO CNMG120408-PM insert geometry, which is the exact insert geometry of our experiment, predicted the temperatures to be approximately 1050 °C as maximum temperature [39]. This simulation has been performed for a slightly lower cutting speed (200 m/min) but a higher feed rate (0.35 mm/rev). The lower feed rate of our experiment is equal to ~25 °C decrease of the simulated temperature but the higher cutting speed will result in ~20 °C increase of the temperature [2]. Besides, a standard built-in AISI 4340 workpiece material was used for the simulation, which has a slightly higher hardness (~40–100 HB units) than the workpiece material in this work, 248–302 HB compared to 205 HB. Thus, taking all of this information into consideration it can be estimated that the maximum temperature is slightly lower in our experiment (950–1000 °C) and overall minor differences in temperatures compared to our experiment are therefore expected.

Fig. 4a shows an overview of the cutting edge and the chip after machining. Similar overall wear patterns were created on the rake faces of the three samples. They are due to the chip formation and sliding, thus due to the contact surfaces between the coating and steel (chip), and are in addition to coating properties also of course influenced by the insert chip-breaker geometry. The collected chips from this dry turning had a blueish color due to the formation of a thin layer of oxide on the chip surface (see insert in Fig. 4a), which indicates a temperature on the order of 250–350 °C [2]. Microscopy investigations give that after 2 min of turning, the α-Al_2O_3 layer remains on both the rake and flank faces, except in a narrow region close to the main cutting edge on the flank face, where the underlying TiCN layer is visible, as marked in Fig. 4a.

Higher magnification SEM images of the rake faces of the inserts are shown in Fig. 4b–d. These images were taken in backscattered electron mode and the bright contrast in these images corresponds to adherent workpiece material. The different contact zones, i.e. the sticking, transition and sliding zones, shown as zone I–III, respectively, are visible and marked on these images. The total contact length is almost the same (around 250–300 μm) for all three textured coatings. The length of the sticking zone (zone I), however, is about 20% shorter on Sample (001) compared to the other two samples, and as a result, this sample has wider transition and sliding zones. The lengths of the different contact zones in Samples (012) and (110) are similar, as shown in Table 2.

The amount of adhered workpiece material on the rake face appears to be different in different zones of the three textured coatings. Table 2 shows the area fractions of different contact zones covered by adhered workpiece material, which were measured on high magnification images with a total area of about 1000 μm^2, acquired from each zone. As shown in Fig. 4b–d, most of the workpiece material adheres to zone I. In this zone, Samples (001) and (012) have within errors the same amount of adhered workpiece material, whereas Sample (110) has close to half the amount. In the transition zone II, the amount of adhered workpiece material decreases to roughly half on all three samples, although in some areas only 4% of adhered workpiece material is found on Sample (001). In the sliding zone III, the amount reduces to 2–5% for Samples (001) and (012), while for Sample (110) it reaches 5–12%.

Overall, the amount of adhered workpiece material is significantly different on Sample (110), where the material is more evenly distributed between all three zones, as seen in Fig. 4d.

In order to measure the thickness of the remaining α-Al_2O_3 coatings on the rake face after machining, cross-sections were prepared using FIB milling. The coating cross-sections, at their minimum thicknesses, which were used to estimate the wear rate, are shown in Fig. 5a. The images show a 52° tilted view of the three samples, where different layers of the coating (cross-section), as well as parts of the coating surface on the rake face are visible. The original coating surfaces were protected against ion milling by depositing a Pt-strip on the surface. Fig. 5b shows the crater depth obtained by imaging the cross-sections along the chip flow direction, from the insert edge to the end of the chip/tool contact. The thicknesses of the coatings do not alter greatly from their original thicknesses (dashed line, 0 μm wear) from the insert edge to a distance of about 150 μm, as shown in Fig. 5b. Thereafter, the coating thicknesses decrease to their lowest values inside the crater, before gradually increasing back to zero.

The minimum coating thickness, for all three textured coatings, was observed at the end of the transition zone and the beginning of the sliding zone. This is the location where the crater probably initiates and gradually expands during the machining process (see Fig. 4a). The minimum remaining alumina coating thickness was measured to be about 2 μm in Sample (001) and about 1 μm for both Samples (012) and (110). It is clear from the alumina layer thickness profile of Sample (001) that the crater is shallower compared to Samples (012) and (110) and that for Sample (012), wear has occurred mainly on the top part of the alumina layer where the $\{01\bar{1}2\}$ texture is dominant.

The maximum remaining coating thickness was observed close to the edge of the insert, in the sticking zone, where the original coating

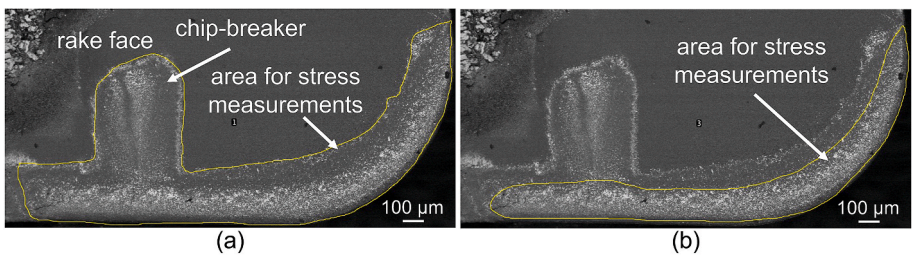

Fig. 3. SEM micrographs showing the contact surface on the rake side of insert indicating the areas considered for stress measurements on (a) total contact area and (b) areas on the edge and sticking zone (bright region). The bright contrast is the adhered workpiece material on the rake face. The chip-breaker is marked.

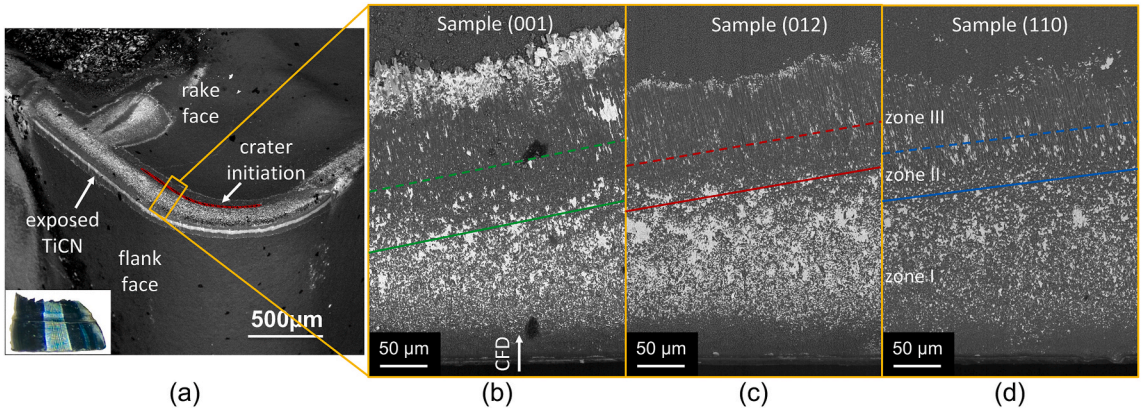

Fig. 4. SEM micrographs showing (a) an overview of the cutting edge and the contact surface on the rake and flank faces in backscattered electron mode. The bright contrast on the rake face shows the adhered workpiece material, while a small bright region on the flank face is due to total removal of the alumina layer exposing the underlying TiCN layer. The initiation of the crater is also marked on the rake face. (b–d) Surface morphologies and adhered workpiece material (bright regions) on the rake face of the three machined CVD α-alumina coatings in backscattered electron mode. The three contact zones are marked and CFD denotes the chip flow direction.

Table 2
Measured lengths of different contact zones and area fraction of adhered workpiece material in different contact zones for Samples (001), (012) and (110).

	Length (μm)			Adhered workpiece material area fraction (%)		
	sticking zone (I)	transition zone (II)	sliding zone (III)	sticking zone (I)	transition zone (II)	sliding zone (III)
Sample (001)	139	66	89	30–40	4–15	2–4
Sample (012)	176	50	66	30–40	~17	3–5
Sample (110)	181	52	58	~20	~12	5–12

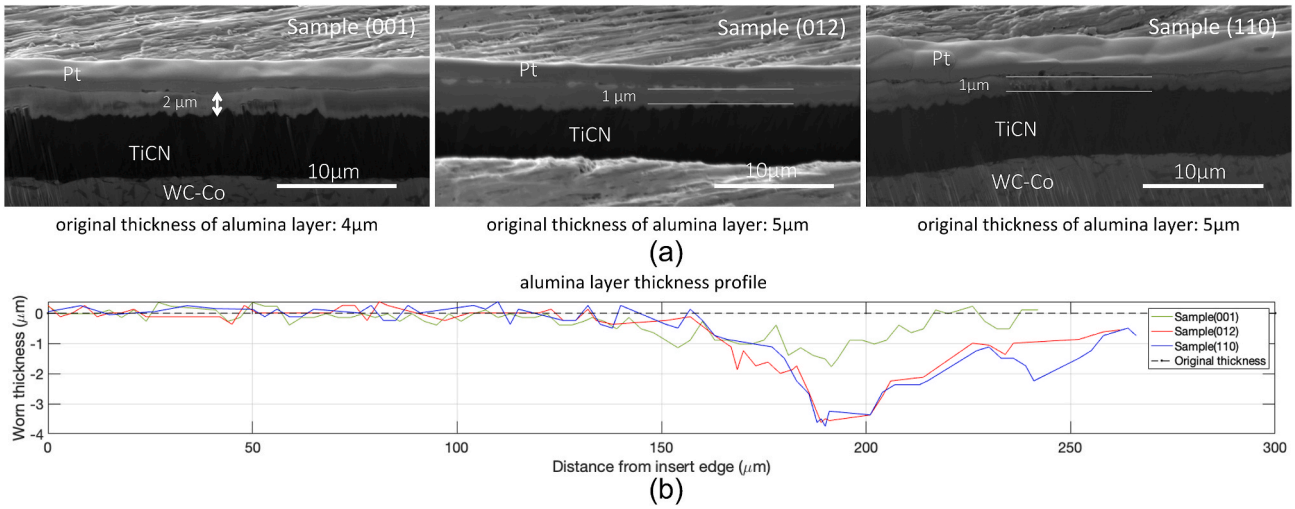

Fig. 5. (a) SEM secondary electron micrographs showing regions with the minimum remaining coating thicknesses after machining. The sample is tilted 52° and the surface is protected by a strip of Pt. The thickness of remaining alumina coating is about 2 μm for Sample (001) and 1 μm for both Sample (012) and Sample (110). (b) Coating thickness profiles were obtained from the FIB cross-sections along the chip flow direction on the rake face. The dashed line shows the original surface of the as-deposited coatings (0 μm).

asperities are still visible. This thickness corresponds to the original coating thickness and was measured to be about 4 μm for Sample (001) and about 5 μm for both Sample (012) and Sample (110). The coating thickness in the crater was obtained after 2 min of continuous turning, giving a wear rate of about 1 μm/min for Sample (001), while it is twice as high (~2 μm/min) for Samples (012) and (110).

3.3. Worn surface appearance

The detailed surface morphology of the three machined textured coatings in the different contact zones are shown in Fig. 6. These surfaces right at the edge of the insert (zone I) for the three samples are shown in Fig. 6a–c. The chip flow direction for all the images is from top to bottom. The grain asperities start to be affected right at the edge of the insert (after the edge rounding region) as the chip starts to make contact and flows over the insert. It is known that the relative contribution of the normal forces applied to the insert is higher in this region [2,19,40], and due to this, the grain asperities exhibit flatter surfaces compared to the original morphology. This is more obvious in Sample (001), in which the asperities have a more topographically flat appearance than the grains in

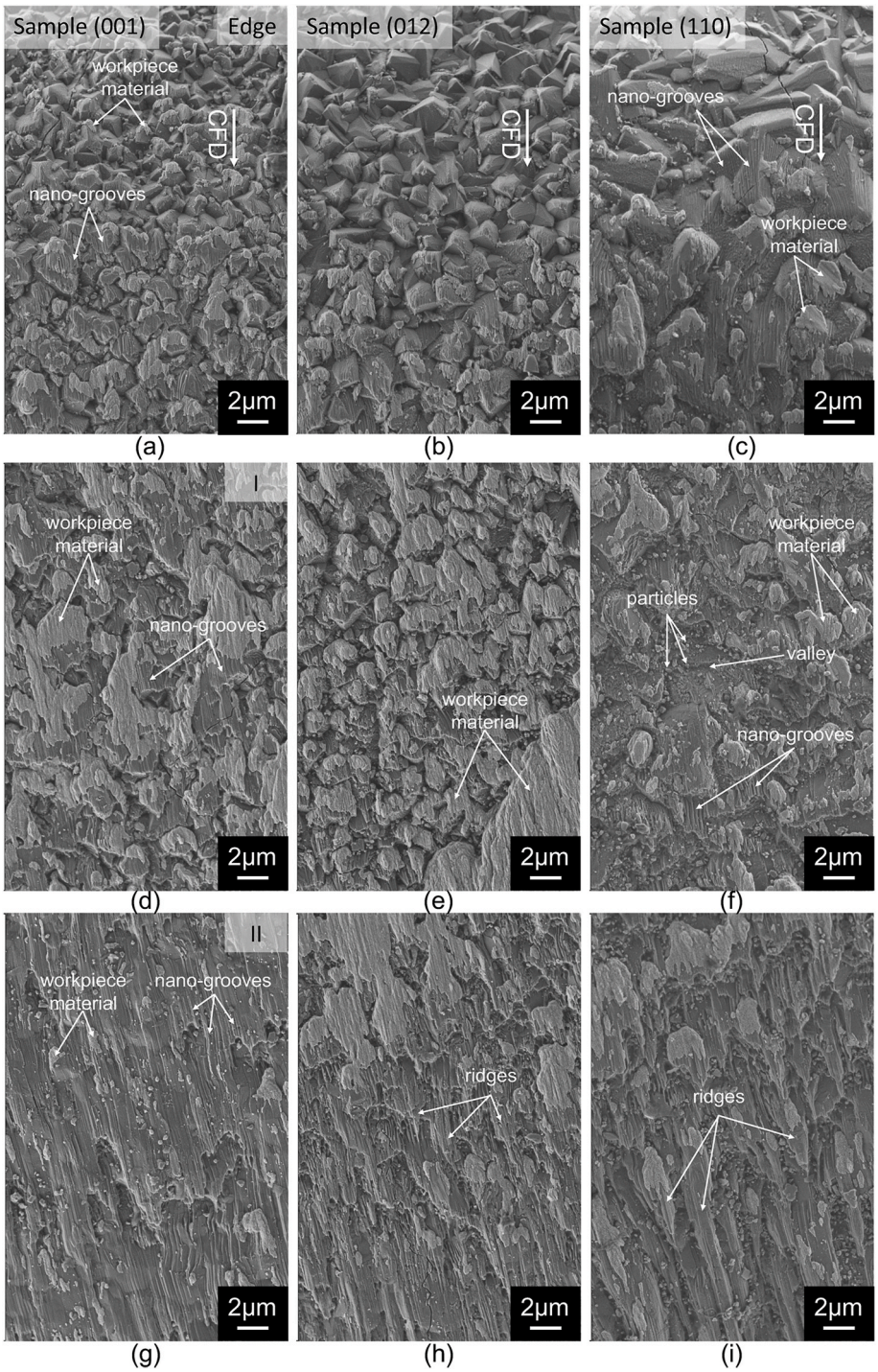

Fig. 6. SEM secondary electron micrographs of the different contact zones on the rake face of Sample (001), Sample (012) and Sample (110) (labeled). The images show the surface morphology at the insert edge in the sticking zone (I) (a–c), inside zone I (d–f), in transition zone (II) (g–i), at the border between zone II and the sliding zone (III) (j–l) and in zone III (m–o). The brighter parts consist of adhered workpiece material. The chip flow direction (CFD) is from top to bottom in all images. Some of the important features are marked.

Sample (012) and Sample (110). Nano-sized grooves start to appear along the chip flow direction on the coating grains, probably caused by the low flow of workpiece material in this region. These grooves create a pattern with flat terraces separated by small steps with heights of 30–60 nm. The terraces are parallel to the coating surface in Sample (001), but inclined in Samples (012) and (110). Adhered workpiece material is observed at the sides of the coating asperities, especially when facing the chip flow direction.

Fig. 6d–f shows the worn coating surfaces further into the sticking zone (zone I). It can be observed in Fig. 6d that for Sample (001) the terraces are elongated over several grains and the original grain asperities are harder to identify. The nano-sized grooves can still be recognized, and although longer, they have the same appearance as at the insert edge. The machined surfaces for Sample (012) and Sample (110) in this region, shown in Fig. 6e and f, exhibit similar surface morphologies as at the insert edge, but appear more worn compared to the insert

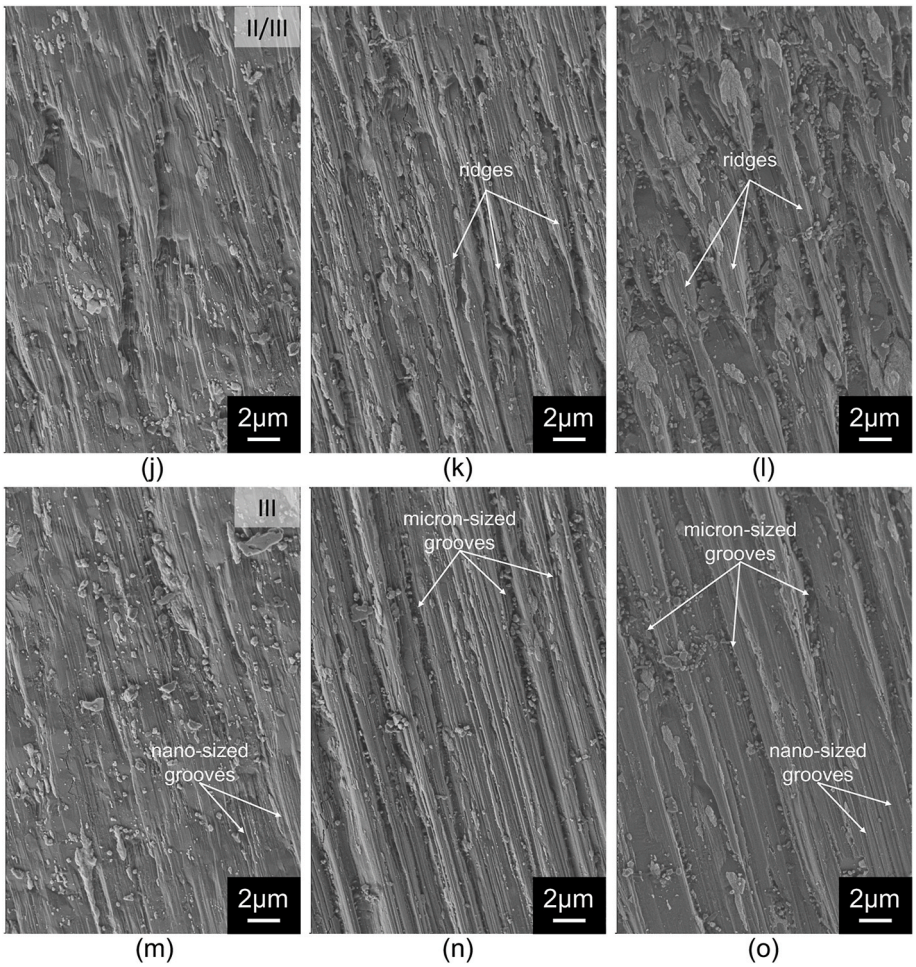

Fig. 6. (*continued*).

edge, which is understandable, given that the degree of wear increases with distance from the insert edge. The original shape of the grains can still be identified in Samples (012) and (110), particularly in Sample (012). Sample (110) exhibits a different surface morphology, where some areas exhibit nano-sized grooves, while some areas consist of valleys with rough surfaces. The height variations are generally 200–300 nm in Sample (001) and 200–550 nm for Samples (012) and (110). The height of nano-terraces is about 50–80 nm in all the samples. In this region, a higher amount of adhered workpiece material is visible on the sides of the grains that face the chip flow (the top side of grains in Fig. 6). However, the areas with adhered material are larger than the ones at the insert edge and sometimes cover the flat surfaces created on top of several grains. A smaller amount of adhered workpiece material can be observed in the Sample (110). Additionally, on this sample, frequent nano-sized spherical particles can be observed that are trapped in the valley-shaped areas. Fewer of these round particles can be observed on Sample (012) and even fewer on Sample (001). Chemical composition investigations of the particles by SEM/XEDS (not shown) revealed that most of these small, round particles consist of Al_2O_3. The particles are thus probably small coating fragments that get rounded as they roll over the surface. The larger particles are oxides of Si–Mg, silicon or calcium that are believed to originate from inclusions in the workpiece material.

Fig. 6g–i shows the surface morphologies of the machined coatings in the transition zone (zone II). Here, all coatings show plastic flow in the direction of chip flow and signs of plastic deformation are evident. The original terraces (zone I) are transformed to larger flat regions, expanding over several grains and containing long grooves (along the chip flow direction) that are nano-sized in width and depth. This effect is most evident for Sample (001), where it is present on almost the entire surface in this region. The nano-sized grooves are also more evident in this sample, probably as a result of the presence of a smoother and flatter surface. The height of the features in this sample is about 200–350 nm, which at a few points the maximum height of the top surface to the valley reaches to 500 nm. For Samples (012) and (110), however, a rough surface is created as a result of an elongation of the asperities created in the previous zone, thus forming extended ridges. In these samples, the height of the ridges to the valleys are between 300 and 700 nm and the detected terraces and steps have a height of around 40–80 nm. These ridges are formed due to plastic deformation and are therefore signs of the activation of several independent slip systems. In contrast to zone I (Fig. 6d), less amount of adhered workpiece material is generally observed in the transition zone (zone II). This is more pronounced on Sample (001), while this difference is only minor for Sample (110). A higher amount of rounded coating fragments and workpiece oxide inclusions can be observed in this zone, especially for Sample (110), where these particles are trapped in the valleys between the ridges, which are quite frequent due to the high roughness of this sample.

The surface morphologies of the machined coatings at the end of the transition zone (zone II) and the beginning of the sliding zone (zone III) are shown in Fig. 6j–l.

This region is typically exposed to the highest temperatures and lowest contact pressures (~0.8 GPa) compared to the other zones [19, 37,41]. This is also the region with minimum coating thickness, as shown in Fig. 5. The plastically deformed surface features are even more

evident in this region for all three samples. For Sample (001) the surface has almost the same morphology as the previous zone, gradually transforming to a more uniformly smooth surface, while for Samples (012) and (110) the ridges of the rough surface are more plastically stretched. The ridges are narrower on Sample (012) with the width of 400 nm to more than 1 μm, which is probably related to the finer grain size compared to Sample (110) that has ridges with the width of 500 to even more than 3 μm. Also, flat surfaces in the areas between the ridges are visible on Sample (110). The long nano-sized grooves that were observed in the previous region can still be seen in this region, especially on Sample (001). The amount of adhered workpiece material decreases even more in this region. Very little adhered workpiece material can be observed on Sample (001) and (012), while the amount on Sample (110) is higher. Similar to the previous region, small particles are visible in this region on the relatively flat surface of Sample (001) and in the valleys of Samples (012) and (110).

The final region of the contact area on the rake face is the sliding zone (zone III), where both the contact pressure and the temperature are lower as compared to zone II. The surface morphologies of the three machined alumina coatings are shown in Fig. 6m–o. In this zone, both the nano-sized and micron-sized grooves are extended over the whole region, in the direction of the chip flow. The micron-sized grooves, which can only be observed on Samples (012) and (110), make the surface rougher on a micron level. The height of these ridges varies from 200 to 800 nm in Sample (012) and is from 400 nm to even 1.5 μm in Sample (110). Sample (001) has by far the flattest and smoothest surface, where no large ridges can be observed. The height of the features in this sample varies between 100 and 250 nm in general, at a few points the top surface to the valley can reach 400–500 nm maximum. The nano-grooves in this sample have a depth of 30–50 nm. Small amounts of adhered workpiece material are visible on the surfaces of all three samples in this region. Spherical coating particles and inclusions can be seen on the surfaces of all samples; they are quite scattered on Sample (001), while they are mainly accumulated in the valleys of Samples (012) and (110).

In order to better observe the differences in surface morphologies of the samples, the chips were investigated. Fig. 7 gives the surface topography of the coatings in the sliding zone (Fig. 7a) and surface topography on the back of the chips (Fig. 7b). By comparing the surface morphology of the back of the chips with the morphology of the coatings in the sliding zone (III), it can be observed that the width of the ridges and valleys created on the back of the chips perfectly match with the features of the coatings in the sliding zone. It can clearly be observed that the flat surface of Sample (001) produces a smooth surface on the chip and rougher surfaces can be observed on the back of the chips for Samples (012) and (110). It is worth also mentioning that the width of the features is larger in Sample (110) compared to Sample (012), which is due to the larger grain size in Sample (110) leading to coarsening of the surface morphology. By drawing a line profile perpendicular to the chip flow direction, the surface roughness of the coatings in zone III and the chips were determined with the 3D dataset generated by Alicona Mex software package utilizing stereoscopic images in SEM. The average roughness of profile (Ra) was determined as 73, 96 and 127 nm for Samples (001), (012) and (110), respectively. The same was done on the coatings in the sliding zone and the Ra values were measured as 74, 102 and 146 nm for Sample (001), (012) and (110), respectively. The 2D

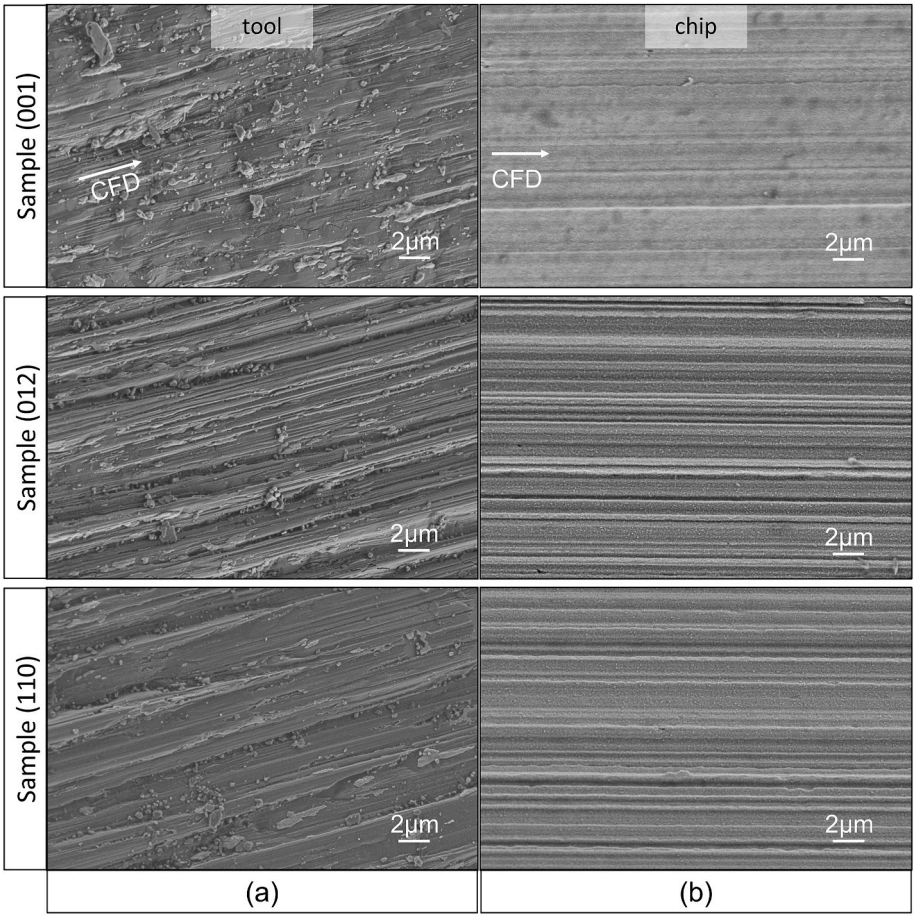

Fig. 7. SEM micrographs of the tool coatings in the sliding zone (III) (a) and back of the collected chips (b) during the dry turning of the workpiece material. The images show that a smooth surface has been created on the chips of Sample (001), while Samples (012) and (110) show a rougher surface with higher ridges and deeper valleys, which are similar to the topography of their respective coatings. The chip flow direction (CFD) is marked for the coatings and the chips.

surface roughness profiles are shown in Fig. 8, where the top profile (Fig. 8a) shows the surface roughness of the chips for the three samples and the profile at the bottom (Fig. 8b) shows the same for the coatings in zone III. It can be observed that the height of the features determined with this method corresponds to the height of the features that were measured on the cross-sections of the coatings in zone III and described in the Fig. 6m–o. Even if this method has a limited accuracy, the numbers clearly show the roughness increase from Sample (001) to Sample (110).

Fig. 9 shows scanning transmission electron (STEM) bright-field micrographs of cross-sections of the α-alumina layer for the three samples. The thin-foil samples shown in this figure were prepared perpendicular to the chip flow direction and in the sliding zone (zone III). This was done in order to investigate the grain-scale surface roughness perpendicular to the ridges and valleys in the sliding zone. A thin layer of platinum was deposited on the surface prior to FIB milling in order to protect the surface from ion-induced artifacts. It is clear from the figure that the alumina layer thickness is larger in Sample (001) even though this sample had a thinner as-deposited alumina layer (4 μm) compared to the other two samples (5 μm) indicating an enhanced performance of this sample during steel turning. It can also be observed that Sample (001) has a more uniform thickness of the alumina layer while the height difference of the ridges and valleys is larger in Samples (012) and (110). The uniform thickness of the alumina layer in Sample (001) produces a significantly smoother surface morphology in this sample. It should be mentioned that the valleys have a smaller width in Sample (012) compared to Sample (110), which could be due to the smaller grain size of Sample (012). Small pieces of the workpiece material (dark particles marked with arrows) can be observed in all three samples that are pressed into the coatings to a depth of around 100 nm. In addition to this, two slag inclusions trapped in the valley can be observed in Sample (110). A mixed layer of the coating and small particles of the workpiece material can be indicated on the ridges of Sample (012) and (110) with a thickness of 40–100 nm and 100–200 nm, respectively. The observed bright layer on the surface of the Sample (110) is an artifact from sample preparation.

To observe the differences in surface morphology of the coatings, especially for Samples (001) and (110), the samples were etched in warm hydrochloric acid to remove the adhered workpiece material on the surface. To gain a three-dimensional sense for the surface topography, the samples were tilted 45° during imaging. Fig. 10 shows an overview of tilted and acid-cleaned machined surfaces in zone I (Fig. 10a and b) and in zones II/III (Fig. 10c and d) for Sample (001) and Sample (110), respectively. A closer inspection of the worn surfaces in zone II reveals that the surface of Sample (001) is rather smooth, especially in the direction of the chip flow. The surface of Sample (001) transforms to an even planer surface as zone III is approached, as shown in Fig. 10c. No large ridge-shaped features can be observed on Sample (001). For Sample (110) there are some ruptured-like regions visible behind flat surfaces, in the direction of the chip flow in zone I, as marked in Fig. 10b. The regions with flat surfaces, together with the ruptured-like areas, generate an overall rough surface in zone I of Sample (110). The surface morphology then transforms to elongated ridge-shaped features in zone III, as shown in Fig. 10d. These ridges are created at the end of the transition zone and are stretched into the sliding zone, leading to a significantly different surface morphology in comparison to the same region in Sample (001).

3.4. Terrace formation and rupture

Etched samples, with the adhered material removed, were used to examine the surface topography of the coatings in order to better understand the structure of the created terraces, ridges and ruptured-like regions. Fig. 11 shows the surface at the end of the sticking zone and the beginning of the transition zone (zone I/II) for Samples (001) and (110). The whole surface of Sample (001) has a homogeneous plastically deformed appearance, where the coating is smeared along the chip flow direction. In the same region, Sample (110) exhibits two different surface morphologies. Regions where flat areas are visible, as well as regions with heavily deformed, ruptured-like patches, are shown in Fig. 11 and Fig. 10b. The ruptured-like regions usually follow a flat region and they make up 30–35% of the surface area in this zone. In contrast, only small amounts (<2%) of these ruptured-like areas were observed on Sample (001). The nano-sized grooves, having a similar origin as the terraces, are observed on the entire surface of Sample (001), while on Sample (110) they can only be observed in the flatter areas.

Terraces are more visible close to the insert edge, where they seem to be created at the early stages of contact between the workpiece material

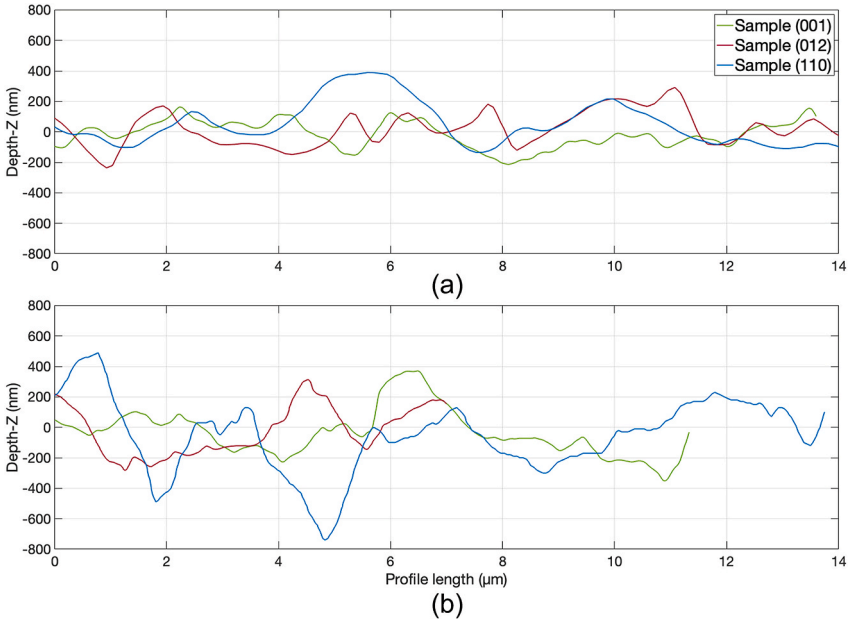

Fig. 8. 2D surface profiles of the back of the chips (a) and the coatings in the sliding zone (zone III) (b) of the three Samples (001), (012) and (110). The line profiles were drawn perpendicular to the chip flow direction.

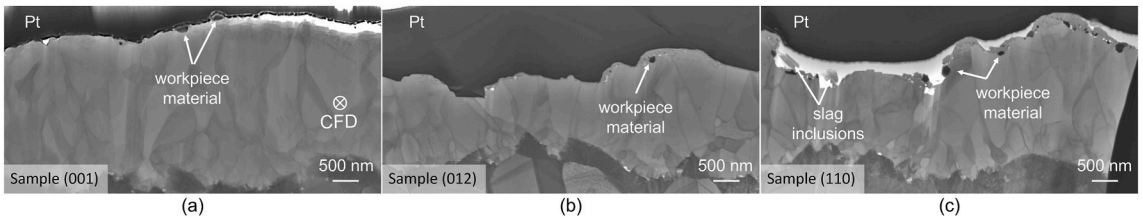

Fig. 9. STEM micrographs showing cross-section of the alumina layer in (a) Sample (001), (b) Sample (012) and (c) Sample (110) in the sliding zone (zone III). A Pt layer is deposited on the surface to protect the surface from ion milling. Some adhered workpiece materials and slag inclusions are marked with arrows. Chip flow direction is perpendicular to the cross-section as marked in Sample (001).

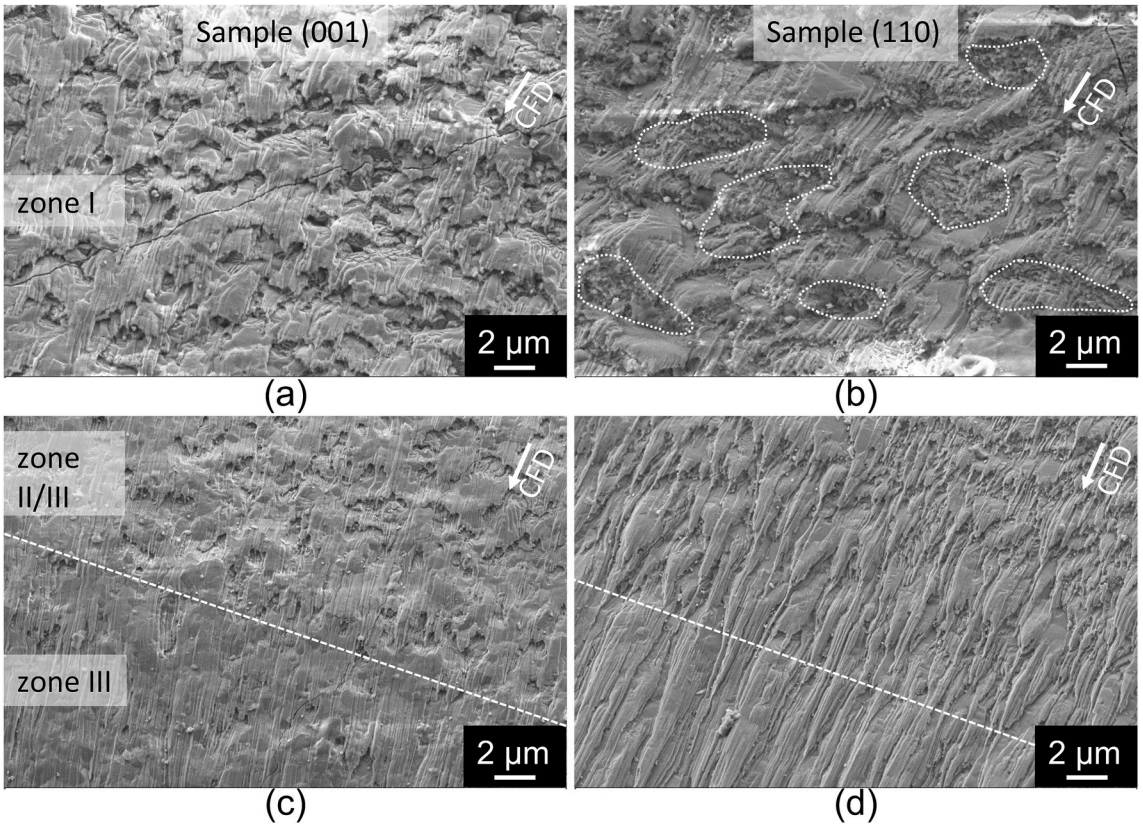

Fig. 10. SEM micrographs of contact zones I (sticking zone) and III (sliding zone) of Samples (001) and (110) tilted 45°. The micrographs show (a–b) the sticking zone (zone I) with ruptured-like areas marked and (c–d) the boundary region between the transition and sliding zones (zone II/III). The adhered workpiece material was removed by chemical etching. The chip flow direction (CFD) is indicated.

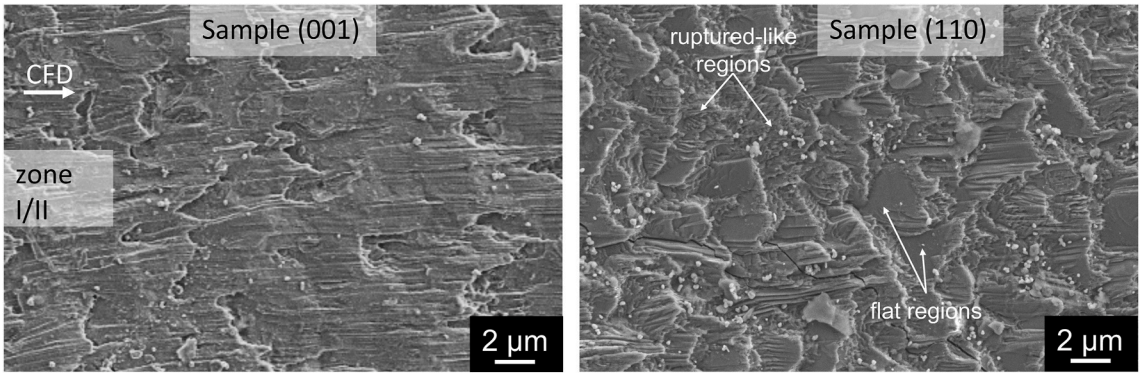

Fig. 11. SEM micrographs of etched coatings showing the surface morphology of Samples (001) and (110). Different surface topographies can be observed for the two textures, where Sample (001) has a more uniform and deformed surface, while some flat and ruptured-like regions can be observed on Sample (110). The arrow shows the chip flow direction (CFD).

and the coating asperities. Fig. 12 shows these terraces in higher magnification. As mentioned above, on Sample (001) the terraces are parallel to the surface, while they are inclined on Samples (012) and (110). The difference in angle for the terraces is probably due to the crystallographic facets with different orientations depending on coating texture. Some regions (marked in Fig. 12c) on Sample (110) do not exhibit terraces, but rather a rounded, uneven surface.

The majority of the terraces are parallel to the surface on Sample (001), but some tilted terraces can also be observed, see Fig. 13. Since Sample (001) has a strong (0001) texture, almost all grains are highly oriented towards <0001>. However, as the texture is not perfect, some grains may be slightly inclined, which would then generate a tilted terrace. Some dimensions of the terraces are measured and marked for Sample (001) in Fig. 13. The height of the terraces is about 40 nm. Tilted terraces are generally observed on Sample (012), as shown in Fig. 13. Inclined terraces, similar to Sample (012), are visible in Sample (110) in the regions where flat surfaces are located. These regions are mostly followed by a ruptured-like region, which is clearly visible in Fig. 13. Cracks visible in this image were probably formed during the cooling of the coatings in the CVD process in the hot reactor.

4. Discussion

4.1. General

The present study was designed to understand the α-alumina layer response during steel turning. Emphasis was put on having the same machining conditions including, workpiece material, insert geometry, edge radius to try to eliminate all parameters except the coating crystallographic texture. The results showed that the developed surface morphology of the contact area on the rake face was altered for different textures. This was found to be dependent on the mechanical deformation mechanisms of the different crystallographic orientations and their ability to plastically shear and deform. We observe the formation of long and parallel ridges, which starts to appear at the end of zone II (transition zone) and continues to zone III (sliding zone), as shown in Fig. 6j–o. Such deformation leads to ductile and/or brittle fracture of small pieces from the deformed ridge-like asperities (micro-chipping) of the coating on the tool rake face. These fractured coating particles, mixed with pieces of the workpiece material, may develop a thin layer of nano-crystalline alumina on the surface [18]. As previous studies have also reported, wear of CVD α-alumina coatings appears to occur by plastic deformation of the surface, followed by removal of deformed material [8,13,14,19,22,42].

In addition, grooves with different sizes are present on the surface, parallel to the chip flow direction. Nano-sized grooves can be observed on all samples and in all three zones. They appear to be linked to the terraces formed at the insert edge, while further away from the insert edge (zone I and II), when the shear forces increase, the long and nano-sized (in width) grooves appear along the chip flow direction. Since these grooves seem to have the same origin as the terraces, this implies that the nano-sized grooves are connected to the crystallographic characteristics of the grains and are not mainly caused by abrasion, since they are visible already in zone I, close to the insert edge, where the chip flow is very limited. The origin of these grooves is discussed in more detail below.

The length of chip/tool contact area is the same for three textured samples, which is probably connected to the geometry of the insert. The length of different zones is, however, different for Sample (001). This sample has longer transition and sliding zones, probably because the wear occurs closer to the insert edge in this sample, which has been reported to be dependent on the original surface topography [43]. The alumina layer thickness profiles of the coatings (Fig. 5b), show that the crater is shallower in Sample (001), resulting in a more gradual thickness variation and thus, a lower wear rate, while in other samples the craters appear deeper implying a more detrimental type of degradation. These variations in local degradation are more related to the texture of the coatings than to other factors like grain size, as Samples (012) and (110) have equal wear rates, but significantly different grain sizes. In addition, the reported (room temperature) nano-indentation hardness for different textures of CVD α-alumina coatings show that (0001) and $\{01\bar{1}2\}$ textures have a similar hardness of 26.4 ± 1.1 GPa, slightly higher than the $\{10\bar{1}0\}$ texture (24.4 ± 1.4 GPa) [44]. This also indicates that the effect of hardness of different textures on the wear behavior would be marginal since $\{01\bar{1}2\}$ and $\{11\bar{2}0\}$ textures show similar crater depth and larger than (0001) texture. It should also be mentioned that since the turning operation and the degradation of the coatings occur at elevated temperatures, it is the hot hardness that is more important in our experiment than the room temperature hardness.

The contact surfaces are partly covered by workpiece material that is adhered mostly on the side of the asperities that face the chip flow, as shown in Figs. 4 and 6. The amount of adhered workpiece material is nearly the same in Samples (001) and (012) and is mainly located in zone I, but it is lower for Sample (110). In this sample, the workpiece material is also more evenly distributed over the three zones. The observed differences could be due to the differences in the original and the developed surface roughness on the coatings during the turning operation, as more uniformly distributed workpiece material has adhered to a rougher surface. The reason for this could be that in a rough-surfaced coating, the mechanical interaction between the workpiece material and the coating surface increases, i.e. the shear stresses, at the transition and sliding zone, which results in adhesion of soft workpiece material on the side of asperities facing the chip flow. This is especially prominent in the transition and sliding zones on Sample (110), which developed a rougher surface in these regions, especially compared to Sample (001). This is also in line with prior studies that linked the amount of material transfer to the topography of the surface [43,45].

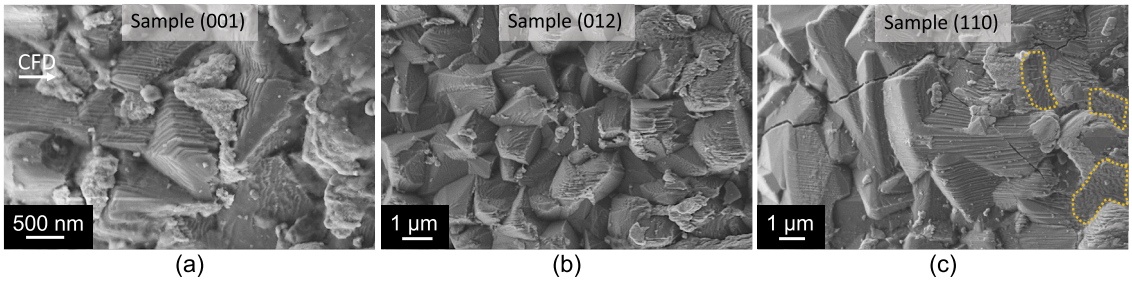

Fig. 12. SEM micrographs of the worn coatings close to the edge of the inserts. Terraces can be observed on all three samples and are created in the direction of chip flow, which is from left to right (labeled CFD). Terraces are parallel to the surface on Sample (001), while they are tilted on Samples (012) and (110). Some regions on Sample (110) (marked) do not form terraces.

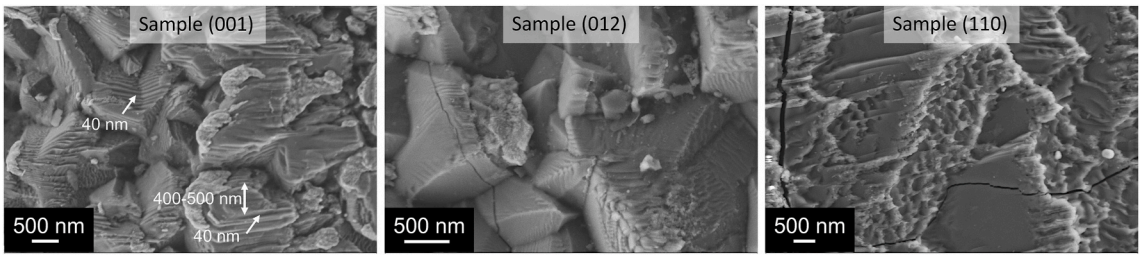

Fig. 13. SEM micrographs of worn grains in zone I (sticking zone). The dimensions of some of the steps and terraces are marked with arrows. Smooth surfaces followed by a ruptured-like area can be observed on Sample (110).

4.2. Nano-scale terrace formation

Terrace-shaped surfaces are evident very close to the edge of the insert where the chip begins to make contact with the tool, as seen in Fig. 12. The terraces (steps some 40 nm high) are visible in all three textured coatings, and to the best of our knowledge, they have not been reported before. What is clearly noticeable on Sample (001) is that most of the terraces have the larger facets parallel to the surface, while on Samples (012) and (110) they are inclined. It is probable that these variations in terrace angle are related to particular crystallographic facets. More specifically they are believed to be basal planes of α-alumina, since these planes are parallel to the surface in (0001)-texture and inclined in $\{01\bar{1}2\}$ and $\{11\bar{2}0\}$-textures with respect to the coating surface. This means that the terraces are influenced by grain orientation and therefore by coating texture. The high normal forces, induced by the chip contact, make cleavage of the coating grains improbable, and plastic flow on certain slip planes (such as basal planes) should in this part of contact zone I be very limited.

At the insert edge, the high temperatures generated by deforming the workpiece material and the very limited flow of workpiece material occurring at the insert edge during the machining operation might induce chemical reactions between the relatively soft and hot workpiece material and the coating. The hot workpiece material in contact with the grain asperities can create an etching effect, generating low energy surfaces in the shape of terraces, extending along with the slowly advancing workpiece flow, i.e. the chip flow direction, as seen in Fig. 12. Some grains on Sample (110) do not form terraces, as shown and marked in Fig. 12. This can be due to the local rotation of the $\{11\bar{2}0\}$-fiber textured grains. When the basal planes are (almost) perpendicular to the chip flow direction it would be virtually impossible to form basal plane terraces. It may be the case that the grains not forming terraces are the cause for the initiation of the ruptured-like areas that are visible and marked in Fig. 10b. Thus, grains with certain orientations do not form terraces and are more prone to rupture.

Further away from the insert edge, the contribution of shear forces, as well as the flow of chip material, increase. These conditions make it possible to shear some of the grains on particular crystallographic planes. The flat surfaces extended over more than one grain in Sample (001), as shown in Fig. 6d. This can imply that the grains were sheared along their basal slip planes. For Sample (110) however, flat surfaces can only be seen on some of the grains, while others show ductile fractures, creating lots of coating debris, as visible in Fig. 6f. In this sample, at the end of zone I (Fig. 11), where the contribution of shear forces is higher, more of the sheared grains creating flat facets can be observed.

4.3. Micron-scale abrasive wear

Abrasion due to hard oxide inclusions and other particles is an important wear mechanism, particularly when machining untreated steels containing non-metallic inclusions. The workpiece material used in this study is a bearing steel, which contains oxide inclusions, e.g. calcium oxide and aluminum silicon oxide. Previous studies [26,42,46] have reported that the large number of grooves on alumina coatings are connected to the high number of inclusions and hard particles in the steel workpiece materials. It is striking that no such micron-sized, deep grooves are observed on Sample (001), which is quite opposite to Sample (110), although the same type of workpiece material and cutting conditions were used in both cases. Contrary to expectations, these micron-sized grooves present between the ridges cannot be solely due to the abrasion of hard particles originating from the workpiece material, since these grooves cannot be observed on Sample (001). Furthermore, the micron-sized grooves are quite well-arranged, with nearly the same spacing, and they are evenly dispersed across the whole depth of cut on the rake face, which makes them unlikely to have formed by abrasion of randomly distributed inclusions in the workpiece material. These results provide support for the hypothesis that the ridges and grooves visible in the sliding zone (zone III) of Samples (012) and (110) are mostly the results of the surface topography observed in zones I (sticking zone) and II (transition zone), but with a more elongated appearance in zone III due to extensive plastic deformation, which is treated in more detail in the next section. Limited abrasion can occur, mainly caused by coating debris, especially of Samples (012) and (110), as micro-rupture of these coatings occurring in zone I produces small and hard particles that later can abrade the coating.

4.4. Plastic deformation

Examinations on the rake face of the three textured CVD α-alumina coatings revealed severe plastic deformation on the surface of all samples starting in the transition zone (zone II). This type of plastic deformation has been reported to be limited to the near surface region and does not extend further than about 500 nm beneath the surface and for this reason, the term ‘discrete plastic deformation’ was assigned to this process [13]. Two different surface morphologies resulting from plastic deformation can be observed mainly in zone II/III (transition/sliding zone). One is a flat-like surface in zone II/III of Sample (001), which is as probably a result of homogeneous plastic flow of the coating near the surface. The other is the rougher surfaces observed in zone II/III of Samples (012) and (110), which contain long ridges that are believed to have formed as a result of plastic deformation of asperities, followed by rupture of the ridge tails. It has previously been hypothesized that such ridge formations should be the result of plastic deformation-induced necking of asperities [22], since the requirement for multiple-slip is fulfilled above 750 °C.

It was reported for untextured coatings that ridges only form at high cutting speeds and that the number of ridges increased with increasing cutting speed [24]. In this study ridges were mainly observed on Samples (012) and (110), even though the same cutting speed was used for all three samples. Therefore, it seems likely that these results are due to differences in conditions for plastic deformation for the different textures. The shear stress on a slip system produced by the compressive stress due to the cutting forces can be calculated for the differently oriented grains, and is given by the Schmid factor (m), $0 \leq m \leq 0.5$. Considering basal slip, we reported that m values approach 0.5 for most grains in the transition zone of Sample (001) [33], which means that

basal slip can easily occur in these grains.

In this work a homogeneous and flat-like surface morphology was found in the transition zone for Sample (001). For the other two samples, Sample (012) and Sample (110), the m value distributions are reported to be wide for the three most probable slip systems, which are $\{0001\}<11\bar{2}0>$ (basal), $\{11\bar{2}0\}<1\bar{1}01>$ (prismatic 1) and $\{11\bar{2}0\}<1\bar{1}00>$ (prismatic 2). It can be noted that only some grains have high m value for both basal and the two prismatic slip systems, while other grains have really low m values [33]. This means that the shear stress necessary for arbitrary plastic deformation in the transition zone can only be reached in some grains in Samples (012) and (110), but not in all. The stress level in these grains will be higher than that calculated for a flat surface since the load carrying area is small due to the surface roughness developed in zone I. It has been estimated that CRSS at temperatures around 900 °C for the basal plane is about 240 MPa and for the prismatic plane is about 390 MPa [19]. Considering the estimated stresses and temperatures in our experiment, it can be noted that the maximum resolved shear stress reaches around 550 MPa ($0.5{\cdot}\sigma$) on average over the contact surface and around 1300 MPa in the sticking zone. Of course, the contact pressure at the asperities is larger, and its magnitude could vary greatly between samples. A flatter surface in Sample (001) results in fewer protruding asperities (Fig. 9a), allowing the pressure to be distributed over a larger area resulting in relatively low contact pressure, a smoother chip surface (Fig. 7b), a thinner sub-surface deformation layer, and a lower chip temperature [43]. While, in the other two samples, a larger height difference between the ridges and valleys causes the stress to be extremely high on the protruding asperities, and this will continue as the process is self-generating. Consequently, plastic deformation can occur even in grains with a much lower Schmid factor m than 0.5. It was reported from our previous work [33] that Samples (012) and (110) have a wide range of m-values for basal and the two prismatic slip planes, which means that some grains can have a high Schmid factor for certain slip systems. Considering the high applied stresses and the high Schmid factor for these grains, the capability of the grains to plastically deform would be high and this is probably the reason why extensive plastic deformation can occur in those grains in zone II/III (transition/sliding), suggesting activation of several slip systems, including those requiring a high critical resolved shear stress (CRSS). The elongated ridges formed in these samples, as seen in Fig. 6k–l, can therefore be related to a deformation of neighboring grains with high m-values. In Sample (001) all grains have high Schmid factors for basal slip system producing a single glide, homogeneous type of plastic deformation, without forming ridges or truncation of the ridges, as seen in Fig. 6j. The slightly coarser microstructure and particularly wider ridges in Sample (110) compared to Sample (012) could be due to larger grain sizes in Sample (110).

In summary, plastic deformation, micro-rupture, abrasion and chemical reactions have all been recognized as mechanisms involved in crater initiation of α-Al_2O_3 coatings during dry high-speed cutting operations used in this work. It was discovered that these wear mechanisms have varying degrees of influence on different textured coatings. For (0001)-texture the main wear mechanisms are attributed to homogeneous plastic deformation, while for $(01\bar{1}2)$ and $(11\bar{2}0)$ textures the main wear mechanisms were attributed to extensive plastic deformation in a limited number of grains, causing rupture (micro-rupture) and abrasion. Chemical reactions and abrasion are present in all textured α-Al_2O_3 coatings but are considered to be less important for crater initiation. However, abrasion is more dominant for $(01\bar{1}2)$ and $(11\bar{2}0)$ textures, since more small, hard particles, of coating debris, are formed due to the micro-rupture of these coatings. However, it appears that abrasion is not the wear rate-determining factor. The effect of a larger grain size is mostly observed as the formation of wider ridges and valleys, and a coarser microstructure in general, while the effect on wear rate is limited in this work.

5. Conclusions

Worn textured CVD α-Al_2O_3 coated cemented carbide cutting tool inserts were analyzed after a dry turning of a bearing steel with the focus on the crater wear mechanisms of three textured CVD α-Al_2O_3 coatings. It was observed that:

- The wear rate of the (0001)–textured coating is half of the $(01\bar{1}2)$ and $(11\bar{2}0)$–textured coatings. This is due to homogeneous plastic deformation in the (0001)–textured coating and the generation of a flat contact surface.
- The amount of adhered workpiece material is the same on the (0001) and $(01\bar{1}2)$–textured coatings, within errors, and is much larger in the sticking zone compared to the other zones. On the $(11\bar{2}0)$–textured coating the amount of adhered material is only half of that on the two other coatings, and the material is more evenly distributed across the three zones.
- In the sticking zone, especially at the insert edge, terraces and nano-grooves are formed presumably by chemical etching of the coatings, due to high normal forces and a low flow of workpiece material, thereby exposing low energy facets, such as (0001). Further away from the insert edge, the nano-grooves seem to be elongated terraces and the appearance of these features are linked to the grain orientations and therefore to the coating textures. Shearing of the grains, probably along their slip planes, creating flat facets and micro-rupture of the $(01\bar{1}2)$ and $(11\bar{2}0)$–textured coatings, is probably occurring in this zone, creating small hard particles and a rough surface.
- In the transition zone, plastic deformation occurs due to higher local temperatures and shear forces. A homogeneous, single glide plastic deformation occurs in the (0001)-textured coating, resulting in the development of smooth and flat surface morphology, while a heterogeneous plastic deformation of the $(01\bar{1}2)$ and $(11\bar{2}0)$–textured coatings result in the creation of long ridges and valleys producing a rough surface. There was no evidence of ridge formation owing to abrasion of inclusions from the workpiece material. However, abrasion of micro-ruptured, small coating particles created in the sticking zone of the $(01\bar{1}2)$ and $(11\bar{2}0)$–textured coatings can also be the cause for the higher wear rates of these coatings.
- In the sliding zone, the surface morphology in the previous zone is further developed. The smooth and flat surface of the (0001)–textured coating results in the creation of a shallow crater and low wear rate. The deeper craters and higher wear rates of the $(01\bar{1}2)$ and $(11\bar{2}0)$–textured coatings are connected to the heterogeneous plastic deformation and associated abrasion of their rougher surfaces. The formation of micron-sized grooves in $(01\bar{1}2)$ and $(11\bar{2}0)$–textured coatings cannot be attributed solely to abrasion of inclusions from workpiece material.
- The impact of coating texture on the relevant degradation mechanisms, and as a result, on the amount of wear, is significant, while the effect of grain size seems to not influence the wear rate significantly during the present cutting conditions. However, it does influence the coarseness of the surface morphology by the larger width of the formed ridges.
- The outcome of the performed investigation is that the mechanical response of the three various crystallographic textured coatings is very different. All textures undergo plastic deformation while Sample (012) and (110) also undergo ductile fracture of individual grains. Sample (001) develops a smooth wear surface that is affected by basal glide. In contrast to previously published machining articles, there was no scratching or abrasive wear from non-metallic inclusions in the steel. Thereby, it would be quite interesting to investigate this further by increasing the degree of (0001) texture and thus aligning the basal slip planes and then comparing the results in steel turning.

Credit author statementfi

Siamak Shoja: Conceptualization, Writing – original draft, Methodology, Formal analysis, Investigation, Data curation, Project administration. **Susanne Norgren**: Supervision, Conceptualization, Methodology, Visualization, Design of machining test, Writing – review & editing, Resources, Funding acquisition. **Hans-Olof Andrén**: Supervision, Conceptualization, Methodology, Writing – review & editing, Formal analysis. **Olof Bäcke**: Conceptualization, Project administration. **Mats Halvarsson**: Supervision, Conceptualization, Methodology, Writing – review & editing, Validation, Funding acquisition.

Declaration of competing interest

The authors declare that they have no known competing financial interests or personal relationships that could have appeared to influence the work reported in this paper.

Acknowledgements

The authors would like to thank Swedish Foundation for Strategic Research (SSF) for their financial support via the contract ID16-0048. This work was performed in part at the Chalmers Materials Analysis Laboratory, CMAL. We would like to acknowledge Dr. Linus von Fieandt and Dr. Jan Engqvist from Sandvik Coromant, as well as Dr. Rachid M'Saoubi and Dr. Tommy Larsson from Seco Tools for their valuable discussions and support of this work. We would like to express our gratitude to Dr. Oscar Alm from Seco Tools for deposition of the coatings, as well as for his insightful remarks regarding this work.

References

[1] R.W. Ivester, M. Kennedy, M. Davies, R. Stevenson, J. Thiele, R. Furness, S. Athavale, Assessment of machining models: progress report, Mach. Sci. Technol. 4 (3) (2000) 511–538, https://doi.org/10.1080/10940340008945720.
[2] E.M. Trent, P.K. Wright, Metal Cutting, fourth ed., Butterworth-Heinemann, USA, 2000.
[3] D.T. Quinto, Mechanical property and structure relationships in hard coatings for cutting tools, J. Vac. Sci. Technol.: Vacuum, Surfaces, and Films 6 (3) (1988) 2149–2157, https://doi.org/10.1116/1.575206.
[4] C.J. Chatfield, N.M. Lindström, E. Sjöstrand, Microstructure of CVD - Al_2O_3, J. Phys. Colloq. 50 (C5) (1989) C5-C377–C5-387, https://doi.org/10.1051/jphyscol:1989545.
[5] O. Knotek, F. Löffler, G. Krämer, Cutting performance of multicomponent and multilayer coatings on cemented carbides and cermets for interrupted cut machining, Int. J. Refract. Metals Hard Mater. 14 (1–3) (1996) 195–202, https://doi.org/10.1016/0263-4368(96)83434-2.
[6] R. Bunshah, C. Weissmantel, Handbook of Hard Coatings, Noyes publications, New York, 2001.
[7] B. Lux, C. Colombier, H. Altena, K. Stjernberg, Preparation of alumina coatings by chemical vapour deposition, Thin Solid Films 138 (1) (1986) 49–64, https://doi.org/10.1016/0040-6090(86)90214-2.
[8] S. Ruppi, Deposition, microstructure and properties of texture-controlled CVD α-Al_2O_3 coatings, Int. J. Refract. Metals Hard Mater. 23 (4–6) (2005) 306–316, https://doi.org/10.1016/j.ijrmhm.2005.05.004.
[9] T. Obikawa, A. Kamio, H. Takaoka, A. Osada, Micro-texture at the coated tool face for high performance cutting, Int. J. Mach. Tool Manufact. 51 (12) (2011) 966–972, https://doi.org/10.1016/j.ijmachtools.2011.08.013.
[10] T. Sugihara, R. Kobayashi, T. Enomoto, Direct observations of tribological behavior in cutting with textured cutting tools, Int. J. Mach. Tool Manufact. 168 (2021) 103726, https://doi.org/10.1016/j.ijmachtools.2021.103726.
[11] S. Ruppi, Enhanced performance of α-Al2O3 coatings by control of crystal orientation, Surf. Coating. Technol. 202 (17) (2008) 4257–4269, https://doi.org/10.1016/j.surfcoat.2008.03.021.
[12] R. M'Saoubi, S. Ruppi, Wear and thermal behavior of CVD α-Al_2O_3 and MTCVD Ti(C,N) coatings during machining, CIRP Annals 58 (1) (2009) 57–60, https://doi.org/10.1016/j.cirp.2009.03.059.
[13] P.A. Dearnley, Rake, Flank Wear, Mechanisms of coated cemented carbides, Surf. Eng. 1 (1) (1985) 43–58, https://doi.org/10.1179/sur.1985.1.1.43.
[14] G. Brandt, Flank and crater wear mechanisms of alumina-based cutting tools when machining steel, Wear 112 (1) (1986) 39–56, https://doi.org/10.1016/0043-1648(86)90199-7.
[15] S. Ruppi, M. Halvarsson, TEM investigation of wear mechanisms during metal machining, Thin Solid Films 353 (1) (1999) 182–188, https://doi.org/10.1016/S0040-6090(99)00413-7.
[16] J. Barry, G. Byrne, Cutting tool wear in the machining of hardened steels: Part I: alumina/TiC cutting tool wear, Wear 247 (2) (2001) 139–151, https://doi.org/10.1016/S0043-1648(00)00531-7.
[17] A. Osada, E. Nakamura, H. Homma, T. Hayahi, T. Oshika, Wear mechanism of thermally transformed CVD Al_2O_3 layer, Int. J. Refract. Metals Hard Mater. 24 (5) (2006) 387–391, https://doi.org/10.1016/j.ijrmhm.2005.11.007.
[18] R. Bejjani, M. Collin, T. Thersleff, S. Odelros, Multi-scale study of initial tool wear on textured alumina coating, and the effect of inclusions in low-alloyed steel, Tribol. Int. 100 (2016) 204–212, https://doi.org/10.1016/j.triboint.2016.01.021.
[19] R. M'Saoubi, O. Alm, J.M. Andersson, H. Engström, T. Larsson, M.P. Johansson-Joesaar, M. Schwind, Microstructure and Wear Mechanisms of Texture-Controlled CVD α-Al_2O_3 Coatings, Wear, vols. 376–377, 2017, pp. 1766–1778, https://doi.org/10.1016/j.wear.2017.01.071.
[20] M. Gassner, N. Schalk, M. Tkadletz, M. Pohler, C. Czettl, C. Mitterer, Influence of Cutting Speed and Workpiece Material on the Wear Mechanisms of CVD TiCN/α-Al_2O_3 Coated Cutting Inserts during Turning, Wear, vols. 398–399, 2018, pp. 90–98, https://doi.org/10.1016/j.wear.2017.11.019.
[21] A. Bjerke, A. Hrechuk, F. Lenrick, R. M'Saoubi, H. Larsson, A. Markström, T. Björk, S. Norgren, J.E. Ståhl, V. Bushlya, Onset of the degradation of CVD α-Al_2O_3 coating during turning of Ca-treated steels, Wear 477 (2021) 203785, https://doi.org/10.1016/j.wear.2021.203785.
[22] G.K.L. Goh, L.C. Lim, M. Rahman, S.C. Lim, Transitions in wear mechanisms of alumina cutting tools, Wear 201 (1) (1996) 199–208, https://doi.org/10.1016/S0043-1648(96)07238-9.
[23] A. Larsson, S. Ruppi, Structure and composition of built-up layers on coated tools during turning of Ca-treated steel, Materials Science and Engineering: A. 313 (1) (2001) 160–169, https://doi.org/10.1016/S0921-5093(01)00964-9.
[24] P.A. Dearnley, E.M. Trent, Wear mechanisms of coated carbide tools, Met. Technol. 9 (1) (1982) 60–75, https://doi.org/10.1179/030716982803285909.
[25] P.A. Dearnley, V. Thompson, A.N. Grearson, Machining ferrous materials with carbides coated by chemical vapour deposition II: wear mechanisms, Surf. Coating. Technol. 29 (3) (1986) 179–205, https://doi.org/10.1016/0257-8972(86)90011-3.
[26] G.M. Faulring, S. Ramalingam, Oxide inclusions and tool wear in machining, Metall. Trans. A 10 (11) (1979) 1781–1788, https://doi.org/10.1007/BF02811716.
[27] S. Ramalingam, J.D. Watson, Inclusion chemistry control for machinability enhancement in steels, Mater. Sci. Eng. 43 (2) (1980) 101–108, https://doi.org/10.1016/0025-5416(80)90136-6.
[28] O. Knotek, F. Löffler, W. Beele, G. Krämer, Comparison of abrasion model test results and machining tests with PVD-coated indexable inserts, Wear (1993) 1033–1039, https://doi.org/10.1016/0043-1648(93) 90118–6.
[29] K. Holmberg, A. Matthews, Coatings Tribology: Properties, Mechanisms, Techniques and Applications in Surface Engineering, Elsevier, 2009.
[30] J. Castaing, J. Cadoz, S.H. Kirby, Deformation of Al_2O_3 single crystals between 25°C and 1800°C : basal and prismatic slip, J. Phys. Colloq. 42 (C3) (1981), https://doi.org/10.1051/jphyscol:1981304.
[31] K.P.D. Lagerlöf, A.H. Heuer, J. Castaing, J.P. Rivière, T.E. Mitchell, Slip and twinning in sapphire (α-Al_2O_3), J. Am. Ceram. Soc. 77 (2) (1994) 385–397, https://doi.org/10.1111/j.1151-2916.1994.tb07006.x.
[32] J. Castaing, A. Munoz, D. Gomez Garcia, A. Dominguez Rodriguez, Basal slip in sapphire (α-Al_2O_3), Materials Science and Engineering: A. 233 (1) (1997) 121–125, https://doi.org/10.1016/S0921-5093(97)00056-7.
[33] S. Shoja, O. Alm, S. Norgren, H.-O. Andrén, M. Halvarsson, Calculated and experimental Schmid factors for chip flow deformation of textured CVD α-alumina coatings, Surf. Coating. Technol. 412 (2021) 126991, https://doi.org/10.1016/j.surfcoat.2021.126991.
[34] S. Ruppi, Texture-hardened Alpha-Alumina Coated Tool, 2011. U.S. Patent 7,923,101 B2.
[35] S. Ruppi, Alumina Layer with Enhanced Texture, 2011.
[36] F. Klocke, A. Kuchle, Cutting tool materials and tools, in: Manufacturing Processes 1, Springer, 2011, pp. 95–196.
[37] E. Usui, T. Shirakashi, T. Kitagawa, Analytical prediction of three dimensional cutting process—Part 3: cutting temperature and crater wear of carbide tool, Journal of Engineering for Industry 100 (2) (1978) 236–243, https://doi.org/10.1115/1.3439415.
[38] E.F. Smart, E.M. Trent, Temperature distribution in tools used for cutting iron, titanium and nickel, Int. J. Prod. Res. 13 (3) (1975) 265–290, https://doi.org/10.1080/00207547508942996.
[39] L. Toller-Nordström, J. Östby, S. Norgren, Towards understanding plastic deformation in hardmetal turning inserts with different binders, Int. J. Refract. Metals Hard Mater. 94 (2021) 105309, https://doi.org/10.1016/j.ijrmhm.2020.105309.
[40] E. Usui, T. Shirakashi, T. Kitagawa, Analytical prediction of cutting tool wear, Wear 100 (1) (1984) 129–151, https://doi.org/10.1016/0043-1648(84)90010-3.
[41] T. Obikawa, T. Matsumura, T. Shirakashi, E. Usui, Wear characteristic of alumina coated and alumina ceramic tools, J. Mater. Process. Technol. 63 (1) (1997) 211–216, https://doi.org/10.1016/S0924-0136(96)02626-X.
[42] A. Nordgren, A. Melander, Tool wear and inclusion behaviour during turning of a calcium-treated quenched and tempered steel using coated cemented carbide tools, Wear 139 (2) (1990) 209–223, https://doi.org/10.1016/0043-1648(90)90046-D.
[43] M. Fallqvist, F. Schltheiss, R. M'Saoubi, M. Olsson, J.-E. Ståhl, Influence of the tool surface micro topography on the tribological characteristics in metal cutting: Part I experimental observations of contact conditions, Wear (2013) 87–98, https://doi.org/10.1016/j.wear.2012.11.002.

[44] T. Giovannini, Understanding the deformation mechanisms of CVD alpha-alumina coatings, Imperial College London, 2018.
[45] S. Saketi, M. Olsson, Influence of CVD and PVD coating micro topography on the initial material transfer of 316L stainless steel in sliding contacts – a laboratory study, Wear (2017) 29–38, https://doi.org/10.1016/j.wear.2016.12.003.
[46] M. Fallqvist, M. Olsson, S. Ruppi, Abrasive wear of texture-controlled CVD α-Al_2O_3 coatings, Surf. Coating. Technol. 202 (4–7) (2007) 837–843, https://doi.org/10.1016/j.surfcoat.2007.06.063.